



Article

Numerical and Experimental Analysis of Microparticle Focusing and Separation in Split–Recombination Microchannel

Shuang Chen ^{1,2}, Jiajia Sun ^{2,*}, Zongqian Shi ², Lijie Sun ¹ and Junxiong Guo ¹

- School of Electronic Information and Electrical Engineering, Chengdu University, Chengdu 610106, China; chenshuang@cdu.edu.cn (S.C.)
- State Key Laboratory of Electrical Insulation and Power Equipment, Xi'an Jiaotong University, Xi'an 710049, China; zqshi@mail.xjtu.edu.cn
- * Correspondence: sunjiajia@xjtu.edu.cn

Abstract

Inertial microfluidics has obtained attention for its good performance in microparticle manipulation. It has the advantages of simplicity, high throughput, and a lack of external fields. In this paper, a simple microfluidic device is described, which contains several split and recombination structures. The design takes advantage of microparticle migration based on inertial lift and the Dean drag force. Two forces drive microparticles to move laterally and arrive at equilibrium positions in a split–recombination microchannel. Based on the numerical and experimental analysis, the trajectories of microparticles are described, and microparticles are focused and form two narrow streams. In addition, the focusing of microparticles is enhanced significantly with the increase in angle. Finally, two sizes of microparticles are separated in experiments. The simple device and high throughput offered by this passive microfluidic approach make it attractive in biomedical and environmental applications.

Keywords: microfluidics; inertial lift force; Dean drag force; focusing and separation; microparticle



Academic Editor: Takasi Nisisako

Received: 25 August 2025 Revised: 30 September 2025 Accepted: 8 October 2025 Published: 10 October 2025

Citation: Chen, S.; Sun, J.; Shi, Z.; Sun, L.; Guo, J. Numerical and Experimental Analysis of Microparticle Focusing and Separation in Split–Recombination Microchannel. *Micromachines* 2025, *16*, 1145. https://doi.org/10.3390/mi16101145

Copyright: © 2025 by the authors. Licensee MDPI, Basel, Switzerland. This article is an open access article distributed under the terms and conditions of the Creative Commons Attribution (CC BY) license (https://creativecommons.org/licenses/by/4.0/).

1. Introduction

The microfluidic technique has been widely employed for collecting cells and particles over the past two decades [1,2]. It has attracted attention in many applications, like disease diagnostics, environment monitoring, and food safety [3–5]. In general, microfluidic technology is mainly divided into two categories, including active and passive microfluidics. Active microfluidics use external energy such as dielectrokinetics [6], magnetohydrodynamics [7], magnetic force [8], and acoustic force [9]. Active types can reduce the length of the microfluidic channel. Meanwhile, complex instruments are involved, and biological activity is also affected unexpectedly. Passive microfluidics mainly rely on the geometrical structure of the microchannel, such as inertial microfluidics [10,11], pinched flow fractionation [12], and deterministic lateral displacement [13]. In general, passive microfluidics can achieve high throughput and do not need external energy [14,15].

As one type of passive microfluidic device, an inertial microfluidic device was first proposed by Di Carlo et al. [16], and it gained a lot of attention due to its high flow rate, simplicity, and external field-free operation. Then, Hur et al. [17] prepared a flow cytometer with one inlet, which is split into 256 parallel straight channels. The particles flowed through the channels, and they were focused to one uniform position based on inertial lift forces.

Asghari et al. [18] presented a sheath-less microflow cytometer, and they achieved the single focusing of microparticles at a throughput of 780 particles per s with viscoelastic fluid. Recently, Jia et al. [19] created a novel microfluidic system featuring an ultra-stretchable channel that allows for size-tunable separation based on elasto-inertial effects. Usually, straight channels are suitable for achieving inertial microfluidic focusing [20,21].

The transformation of a straight channel into a split configuration greatly broadens its potential applications. For example, Yap et al. [22] employed a T-junction bifurcation channel and an integrated microheater on one side of the channel in 2009. This design enables a mother droplet to split into two daughter droplets, thereby establishing the intended sensor functionality. Li et al. [23] presented a method for manipulating ferrofluid droplets using a permanent magnet. In a microfluidic chip, the splitting section serves to sort and collect the formed water-based ferrofluid droplets.

In addition to the inertial lift force in the straight channel, Dean drag forces in transverse Dean flow arise from the curved channel structure. Recently, Cruz et al. [24] presented a new type of microfluidics. It exploited inertial focusing in a high-aspect-ratio curved microchannel. In addition, Shen et al. [25] developed a spiral microchannel, which contains several micro-obstacles for particle focusing and separation. The separating of polymeric particles and cells was successfully accomplished. For the prediction and deep analysis of the trajectories of particles or cells, a numerical simulation is applied as an effective tool. Shamloo et al. [26] researched the particle focus in the serpentine channel accurately through a 3D Direct Numerical Solution method. Do et al. [27] presented a developed Immersed Boundary (IB) method solver for modeling inertial particle sorting. Although a variety of devices were designed and performed well in focusing and separation, a gap in designing microfluidic devices exists still. Meanwhile, there are a few complex numerical methods for calculating the inertial lift force and describing the trajectories of particles.

Herein, we present a split–recombination microchannel with several straight channels with different cross-sections. Meanwhile, a computational model was developed to describe the inertial focusing motion of microparticles in the channel. The complete microparticle trajectory was obtained through a numerical simulation, and the analysis of particle migration was carried out. Next, the influence of the flow rate and the shape of the split–recombination structure on microparticle focus was discussed through an experiment. In addition, microparticle separation with two microparticle sizes was investigated as well, and the performance of the designed microchannel was tested.

2. Methods

2.1. Fluid Flow

The flow field in the microchannel, u_f , is governed by the continuity equation and Navier–Stokes equations [28]:

$$\nabla \cdot (\rho \cdot \mathbf{u}_{\mathbf{f}}) = 0 \tag{1}$$

$$\rho(\mathbf{u}_{\mathbf{f}} \cdot \nabla)\mathbf{u}_{\mathbf{f}} = -\nabla P + \mu \nabla^2 \mathbf{u}_{\mathbf{f}} \tag{2}$$

where u_f , ρ , μ , and P are the velocity, density, dynamic viscosity, and pressure of the fluid, respectively.

The fluid flow is described in terms of the Reynolds number. It is controlled by varying the flow rate [29].

$$Re = \frac{\rho U D_{h}}{\mu} \tag{3}$$

Here U corresponds to the average fluid velocity of the inlet. $D_{\rm h}$ (= $2(W_{\rm ch}H_{\rm ch})/(W_{\rm ch}+H_{\rm ch})$) is the hydraulic diameter of the microchannel. $H_{\rm ch}$ and $W_{\rm ch}$ are the microchannel's height and width, respectively.

2.2. Inertial Lift Force

In 1974, Ho & Leal [30] proposed an analytical expression for describing the inertial lift force on the cross-section of a straight microchannel. Inertial lift force formulas are shown in Equations (4)–(7)

$$F_{L} = F_{Ls} + F_{Lw} = (\beta^{2} G_{1} + \beta \gamma G_{2}) \frac{\rho_{f} r_{p}^{4}}{D^{2}} n$$
(4)

$$\beta = |D(\mathbf{n} \cdot \nabla)\mathbf{u}_{p}| \tag{5}$$

$$\gamma = \left| \frac{D^2}{2} (\mathbf{n} \cdot \nabla)^2 \mathbf{u}_{\mathbf{p}} \right| \tag{6}$$

$$u_{\mathbf{p}} = (\overline{\overline{I}} - (\mathbf{n} \otimes \mathbf{n}))u_{\mathbf{f}} \tag{7}$$

In these formulas, β is the shear rate. γ is the shear gradient. G_1 and G_2 are functions of the lateral position of the microparticle. u_p is the particle velocity. D represents the distance between the walls of the microchannel. n represents the unit normal vector of the microchannel wall. \overline{l} is the unit tensor.

2.3. Dean Drag Force

At the bending position of the microchannel, the flow is characterized by the Dean number *De*. It represents the Dean drag force in curved channels [31].

$$De = \text{Re} \times \sqrt{\frac{D_{\text{h}}}{2R}} \tag{8}$$

where *R* is the curvature radius. It is distinct that the Dean number is larger with an increase in Re and with a decrease in R. The expression for the Dean drag force is shown below [32].

$$F_{\rm D} = 3\pi\mu U_{\rm Dean} d_{\rm p} = 5.4 \times 10^{-4} \pi\mu D e^{1.63} d_{\rm p} \tag{9}$$

where $U_{\rm Dean}$ represents the average Dean velocity given by $U_{\rm Dean} = 1.8 \times 10^{-4} De^{1.63}$, and $d_{\rm P}$ is the microparticle diameter. $F_{\rm L}$ and $F_{\rm D}$ both dominate the motion of the microparticle in curved channels.

For a microparticle in a microchannel, it is subject to the viscous drag force [5].

$$F_{\text{vis}} = 3\pi\mu (u_{\text{f}} - u_{\text{p}}) d_{\text{p}} \tag{10}$$

2.4. Microparticle Motion

The microparticle in fluid is driven by inertial lift force, drag force, gravity, and buoyant force. In this model, the Peclet number ($Pe = Lu_p/D$, where L is the characteristic length of the microchannel, and D is the mass diffuse coefficient) is large enough ($Pe \gg 1$) so that the Brownian motion of microparticles is not taken into account [33]. The trajectories of microparticles are governed by Equation (11) based on Newton's second law [34,35].

$$m_{\rm p}\frac{d\mathbf{u}_{\rm p}}{dt} = \mathbf{F}_{\rm dia} + \mathbf{F}_{\rm vis} + \mathbf{F}_{\rm gb} \tag{11}$$

where m_p is the mass of microparticles.

3. Numerical and Experimental Setup

A numerical simulation of the microchannel flow is conducted using ANSYS FLUENT 17.0. Additionally, microparticle motion is simulated using the discrete phase model in

ANSYS FLUENT, which treats microparticles as a discrete phase within a continuous fluid. Microparticle trajectories are computed over time using a transient solver. The microchannel inlet and outlet are assigned velocity and pressure boundary conditions, respectively, with no-slip walls.

In the experiment, 1% (w/v) fluorescent microparticles with diameters of 5 µm and 10 µm (Huge Biotechnology, Shanghai, China) were used to mimic red blood cells and leukocyte, respectively, which were diluted to 0.1% (w/v) by deionized water. Tween 20 (0.5 wt%, Sigma-Aldrich Co., St. Louis, MO, USA) was added into the solution, which can prevent the aggregation of microparticles. A syringe pump (Elite 11, Harvard Apparatus, Holliston, MA, USA) was used in experiments. Images of microparticles were captured by an inverted fluorescence microscope (AE31E, Motic, Xiamen, China). Adobe Photoshop (Adobe Systems Inc., San Jose, CA, USA) and ImageJ 1.53c software (NIH, Bethesda, MD, USA) were used to process and analyze the captured images. The platform of the experiment is shown in Figure 1, including a syringe pump, inverted fluorescence microscope, microfluidic chip, and computer. Image acquisition was performed via digital capture controlled by a computer.



Figure 1. Image of experimental platform.

Microchannels were made by using standard soft lithography techniques. Firstly, SU-8 photoresist (MicroChem, Round Rock, TX, USA) was spun onto a Si wafer at 2600 rpm. After soft baking, the Si wafer was exposed via UV light using a UV KUB2 exposure machine (Kloe, Saint-Mathieu-de-Tréviers, France) under a mask with a certain pattern. Then, the SU-8 mold of the microchannel was obtained by several physical and chemical processes, including post-exposure baking, development, rinsing, and hard baking. PDMS and the PDMS activator (Sylgard 184, Dow Corning, Midland, MI, USA) with a weight ratio of 10:1 were cast onto the SU-8 mold. Then, the layer was peeled off from the SU-8 mold after curing. Inlet holes and outlet holes were made by a puncher. Finally, the layer was bonded to a smooth glass slide by plasma treatment.

4. Results and Discussion

4.1. Distribution of Inertial Lift Force

To describe the trajectories of microparticles in the microchannel, the inertial lift force is calculated by simulation. In the simply straight microchannel shown in Figure 2a, the width W is 200 μ m. The height H is 50 μ m. The length L is 40 mm. The throughput of fluid is 120 μ L/min. Firstly, mesh independence verification is carried out to determine the optimal mesh size and minimize the influence of mesh size on the simulations. Taking the above straight microchannel as an example, a hexahedral element is adopted to discretize the computational domain. By gradually refining the mesh, the amount of mesh in the y-z plane is increased progressively from 100 to 10,000, neglecting effects along the x-axis. Figure 2b shows the flow velocity along the z-axis at the microchannel center (y = 0) with different numbers of mesh. It can be observed that mesh independence for the flow field is

achieved at a mesh count above 400. Similarly, the same method is employed to determine the mesh count in the subsequent simulations.

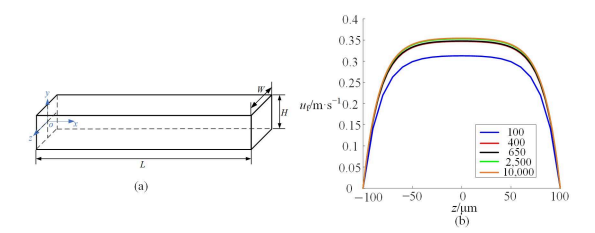


Figure 2. (a) shows a schematic diagram of a straight microchannel; (b) shows the flow velocity along the *z*-axis at x = L/2 and y = 0 with different numbers of mesh.

When y = 0 and x = L/2, G_1 , G_2 , β , and γ in Equation (4) are as shown in Figure 3. The value of G_1 is positive, and G_2 is negative, with both β and γ being negative. Therefore, the coefficients $\beta^2 G_1 + \beta \gamma G_2$ in Equation (4) will have a zero point, which is one equilibrium position of microparticles.

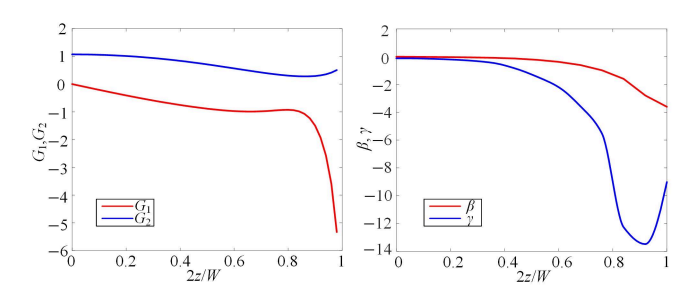


Figure 3. The distribution of parameters (G_1 , G_2 , β , and γ) with 2z/W.

Figure 4 shows the distribution of the inertial lift force acting on microparticles with a diameter of 5 μ m. In Figure 4a, the length of the arrow reflects the actual magnitude of F_L . Hence, it is summarized that F_L near the walls of the microchannel is larger, while in the center of the microchannel, F_L is relatively smaller, and the direction is not even observed. Figure 4b depicts the normalized distribution of F_L . Arrows just reflect the direction of F_L . The particle blockage ratio κ ($\kappa = d_p/H$) is 0.1, and the effect of the surrounding fluid velocity gradient on particle motion becomes neglected. As a consequence, it is expected that microparticles will gather at four corners and the centers of the bottom and top walls in the straight microchannel, in which red balls represent microparticles. In addition, the inertial lift force in the microchannel with a cross-sectional size of 100 μ m \times 50 μ m is calculated in the same way.

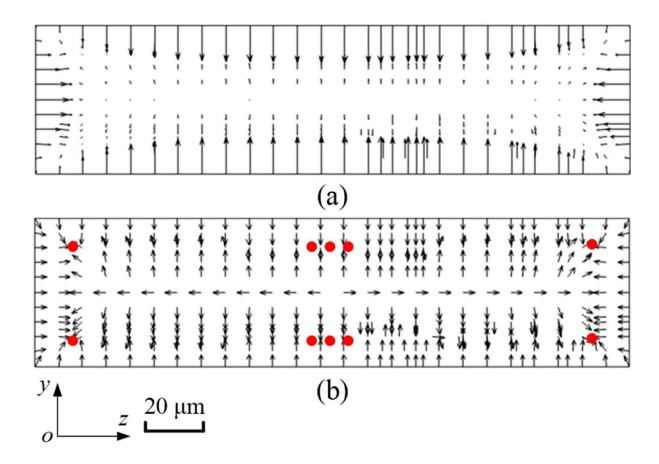


Figure 4. The distribution of F_L acting on microparticles with a diameter of 5 μ m. (a) shows the magnitude of F_L , and (b) shows the direction of F_L .

4.2. Three-Dimensional Focus

A split–recombination microchannel was adopted in experiments, and it is shown in Figure 5. It consists of different cross-sections of straight channels. Taking into account an actual microfluidic chip, the geometric parameters are designed as below. The total length (L) is approximately 40 mm, and the width (W) is 200 μ m. In addition, the length of the diamond structure (l_r) is 600 μ m. The length between two diamond structures (l_s) is 400 μ m. The height of the microchannel is about 50 μ m. In addition, there are 38 diamond structures in the split–recombination microchannel, and the angle θ is 30°, 60°, and 90°.

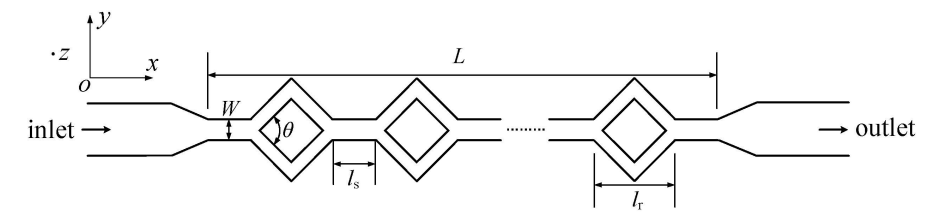


Figure 5. A schematic diagram of the split–recombination microchannel.

The whole trajectory of microparticles is obtained through numerical simulation, as shown in Figure 6a. For a clearer observation of the microparticle distribution, the area within the blue dashed is magnified, as shown in Figure 6c. Figure 6b displays the experimental results achieved with an identical parameter configuration. When the flow rate is 300 μ L/min, it can be observed that 5 μ m diameter microparticles focus into two streams in the split–recombination microchannel from the top view (*x-y* plane). Based on Figure 6b,c, the distribution range of microparticles and accurate positions of microparticle stream boundaries are quantified and plotted in Figure 6d. The width and position of microparticle streams are similar. In contrast to the simulation results, the experimental results show an absence of microparticles near the wall. The scarcity of microparticles observed in the experiments can be attributed to the unstable equilibrium of positions near the wall. This comparison with the experimental results serves as a validation of the simulation model's accuracy.

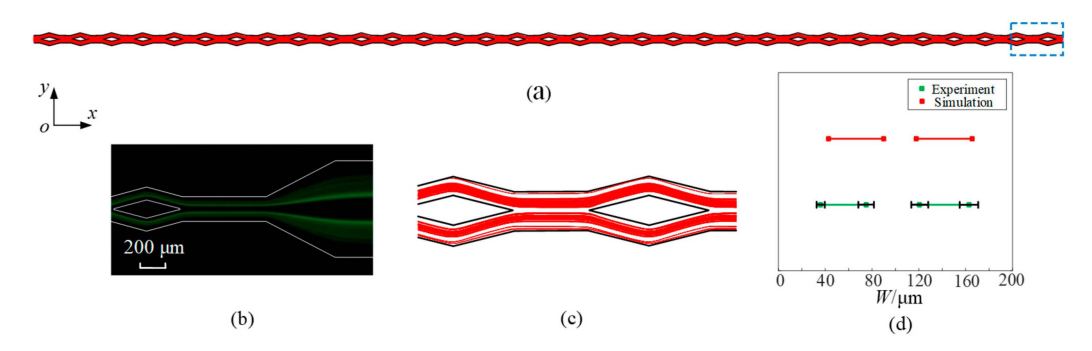


Figure 6. The trajectories of microparticles ($d_p = 5 \mu m$) at a flow rate of 300 $\mu L/min$ by simulation (**a**,**c**) and the experiment (**b**). (**d**) shows the distribution range of microparticles at the microchannel outlet.

Specifically, microparticle migration can be divided into three parts, as shown in Figure 7. Firstly, microparticles are concentrated near the lower and upper walls by $F_{\rm L}$, as shown in Figure 4. When microparticles enter the diamond structure, they migrate to two sides, as shown in Figure 7b. The Dean vortices generated at the bend of diamond structures are shown in Figure 7c. Microparticles move along the vortices. Microparticles exhibit opposing migration patterns depending on their vertical position: those at the midplane move radially outward, whereas those near the top and bottom walls migrate inward. Finally, when microparticles flow out of the diamond structure, they move towards

the center of the microchannel, as shown in Figure 7d. In addition, one particle stream is observed from the side view. Therefore, the conclusion is credible that microparticles are focused into two streams by the split–recombination microchannel.

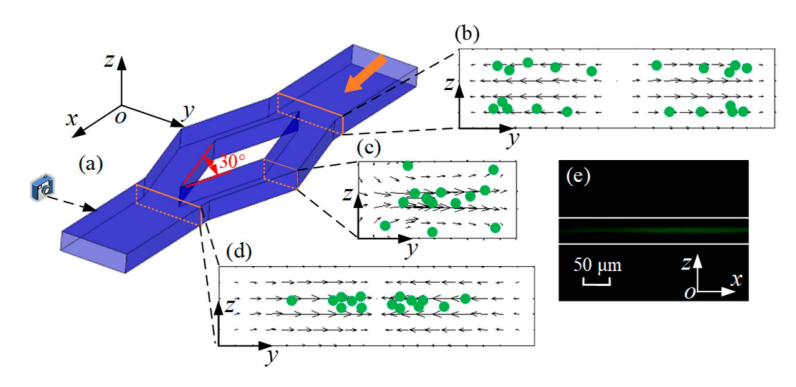


Figure 7. (a) Schematic diagram of three-dimensional microchannel. (b–d) Visualization of cross-sectional microparticle (green dots) migration dynamics and simulation results of velocity vector field (arrows) in y–z plane at flow rate of 300 μ L/min. (e) Image of fluorescent microparticles at outlet of split–recombination microchannel from side view at flow rate of 300 μ L/min.

4.3. Effect of Flow Rate on Microparticle Focusing

As indicated by Equations (4)–(7) and (9), the flow rate significantly influences both the inertial lift and Dean drag forces. Consequently, its effect on the distribution of 5 μm microparticles at the outlet is investigated at rates of 60, 120, 180, 300, and 420 $\mu L/min$ (Figure 8). In the split–recombination microchannel with $\theta=30^{\circ}$, microparticles are slightly focused. As the flow rate increases, it is observed that the focusing of microparticles becomes more apparent. At a flow rate of 420 $\mu L/min$, there are two obvious microparticle streams. However, many microparticles are still scattered in the microchannel.

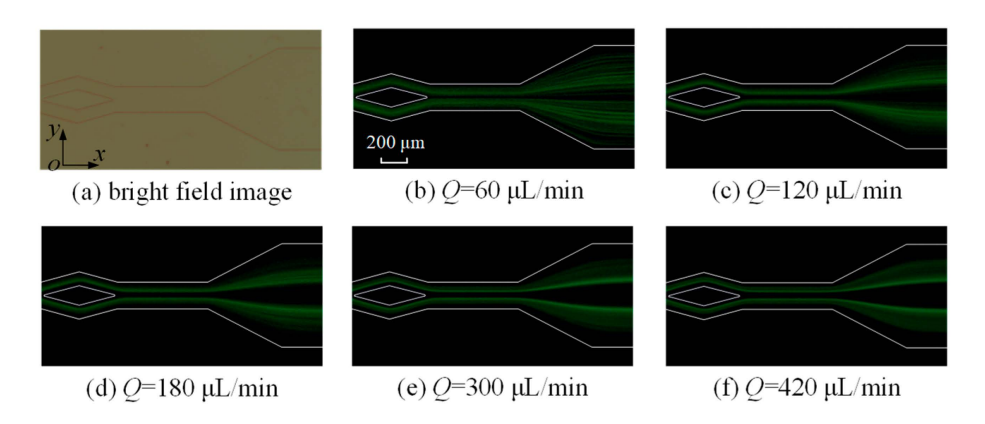


Figure 8. The images of fluorescent 5 μ m microparticles at the split–recombination microchannel's outlet.

An increase in flow rate enhances both the inertial lift and Dean drag forces. Hence, to understand the mechanism of the Dean drag force, Dean vortices are drawn, as shown in the cross-section in Figure 7c. In Figure 9, black arrows represent the vector of fluid velocity. As the flow rate increases from 60 to 180 μ L/min, the cross-sectional fluid velocity becomes greater. It can be deduced that the Dean vortices will be more pronounced, and the Dean drag force will be greater with a higher flow rate. Based on the above trend, it can be concluded that the focusing of microparticles is positively correlated with Dean vortices.

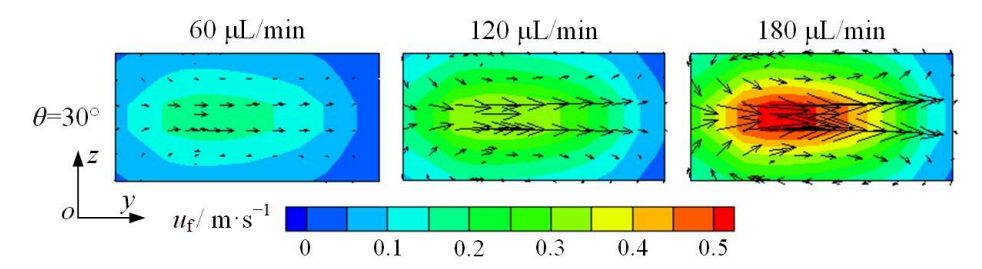


Figure 9. Cross-sectional fluid velocity distribution in the split–recombination microchannel under different flow rates (Figure 7c).

4.4. Effect of Angle θ on Microparticle Focusing

To enhance the effect of Dean vortices on microparticle focusing, the diamond-shaped structure is optimized with angle θ set to 30°, 60°, and 90°. Taking 5 µm diameter microparticles as an example, the focusing of microparticles is improved significantly, as shown in Figure 10(a1–c1). When angle θ is 30°, despite segregating into two distinct streams, microparticles maintain a dispersed state. With the increase in angle, dispersed microparticles disappear, and two microparticle streams are thinner and clearer with θ = 90°.

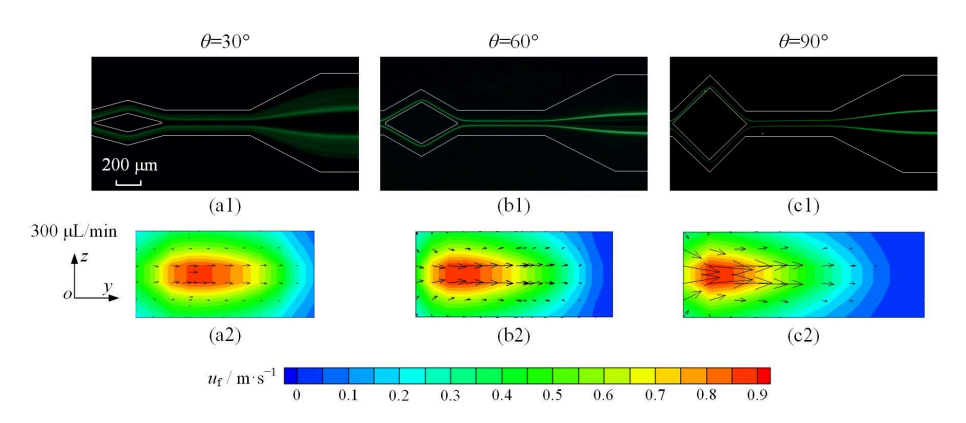


Figure 10. (a1–c1) show fluorescent images of 5 μ m microparticles at 300 μ L/min flow rate, captured at outlet of split–recombination microchannel; (a2–c2) show distribution of fluid velocity at cross-section shown in Figure 7c in split–recombination microchannel with different angles.

For the purpose of causal analysis, the vector of fluid velocity is drawn with different angles (θ = 30°, 60°, and 90°) at the cross-section of the split–recombination structure, which is shown in Figure 10(a2–c2). Despite the velocity contours of a similar magnitude, the peak velocity exhibits a progressive shift toward the inner-wall region as the angle increases. In addition, a significant increase in the fluid velocity vector is observed as the angle reaches 90°. The enhancement in F_D , as per Equation (9), is attributed to the increased flow velocity induced by a larger angle. Therefore, the synergistic action of F_L and F_D produces two sharply focused particle streams in the experiments.

4.5. Microparticle Separation

Finally, two microparticle sizes are co-injected into the microchannel, with their distributions shown in Figure 11. When $\theta=30^\circ$, it can be seen that the 10 μm orange fluorescent microparticles form two thinner streams, while the 5 μm cyan fluorescent microparticles still disperse in the channel. Microparticle separation failed due to the overlap of two types of microparticle distribution.

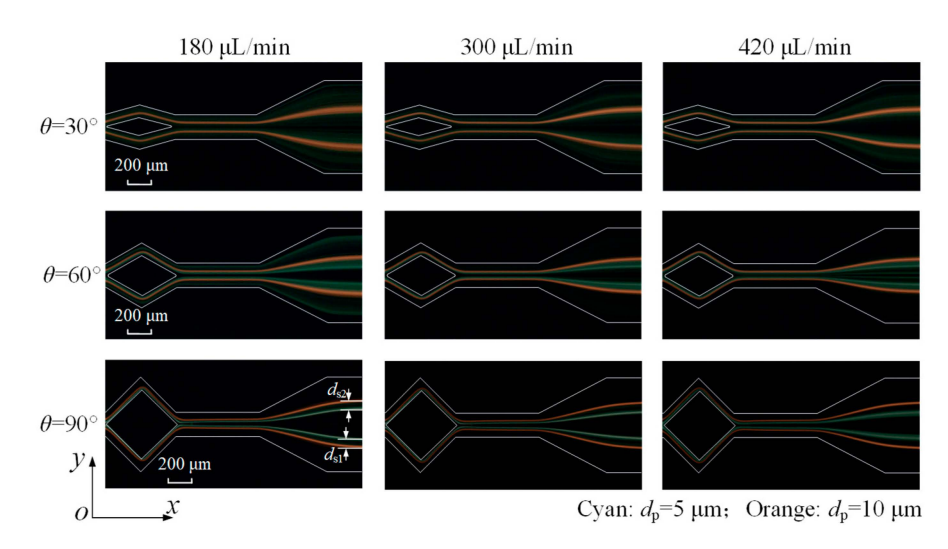


Figure 11. Fluorescent images of 5 μ m (cyan) and 10 μ m (orange) microparticles at microchannel outlet under various flow rates and angles.

At θ = 60°, although the focusing of 5 µm microparticles is significantly improved, they nevertheless fail to form a narrow stream and thus remain unseparated. A 90° angle enables the 5 µm microparticles to be focused into two narrow streams, achieving the separation of both sizes. As a single process, it achieves an increased flow rate for separation based on the experimental results, compared with some studies, as shown in Table 1. Moreover, the 5 µm microparticle streams broaden at 420 µL/min, primarily due to an excessive Dean drag force disrupting the balance and preventing microparticles from maintaining equilibrium.

Table 1. Comparison of performance in this work with several existing works.

	Configuration	Flow Rate	Diameter
Lee et al. [36]	Contraction– expansion	14.5 mL/h ≈242 μL/min	1, 4, 10, 15 μm
Zhang et al. [37]	Serpentine	$350 \mu\text{L/min}$	3, 10 μm
Shrestha et al. [38]	Zigzag	$200 \mu L/min$	3, 10, 15, 20 μm
this work	Split-recombination	$420 \mu L/min$	5, 10 μm

To quantitatively analyze separation performance, the distance between microparticle streams (d_s) is measured and presented as a dimensionless relative value. Its trend is shown in Figure 12, which exhibits an increasing d_s with the rising flow rate. However, beyond a flow rate of approximately 300 μ L/min, the influence of flow rate on d_s diminishes significantly, and the value of d_s plateaus.

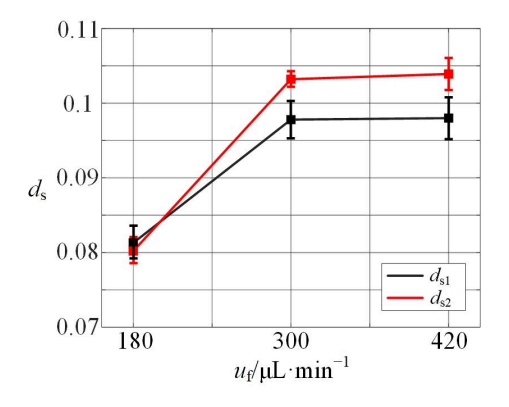


Figure 12. The relative distance of two sizes of microparticles with angle = 90° and different flow rates.

5. Conclusions

In this paper, a split–recombination microchannel incorporating diamond-shaped features is designed and fabricated for enhanced microparticle focusing. Meanwhile, a computational model is developed to describe the inertial focusing motion of microparticles in the split–recombination microchannel, which can reduce experimental waste. By comparing the results of the simulation and experiment, one kind of microparticle will focus two streams in three dimensions. Subsequently, two microparticle streams are thinner and clearer with the increase in flow rate and angles in the experimental results. Therefore, two sizes of microparticles could be separated with a suitable parameter (flow rate = 300 μ L/min; θ = 90°). This work offers practical insights for inertial microparticle and cell focusing and separation, potentially handling samples with high throughput in applications in life, chemical, and material sciences.

Author Contributions: Conceptualization, S.C. and J.S.; Methodology, S.C.; Software, L.S.; Formal analysis, S.C.; Data curation, L.S.; Writing—original draft, S.C.; Writing—review & editing, J.S., Z.S. and J.G.; Funding acquisition, J.S. All authors have read and agreed to the published version of the manuscript.

Funding: This research was funded by National Natural Science Foundation of China, grant number 52307015.

Data Availability Statement: The data that support the findings of this study are available from the corresponding author upon reasonable request.

Conflicts of Interest: The authors state that they have no conflicts of interest.

References

- 1. Lu, X.; Liu, C.; Hu, G.; Xuan, X. Particle manipulations in non-Newtonian microfluidics: A review. *J. Colloid Interface Sci.* **2017**, 500, 182–201. [CrossRef]
- 2. Yin, J.; Wang, Z.; Li, G.; Lin, F.; Shao, K.; Cao, B.; Hou, Y. Characterization of circulating tumor cells in breast cancer patients by spiral microfluidics. *Cell Biol. Toxicol.* **2019**, *35*, 59–66. [CrossRef]
- 3. Ahmed, I.; Iqbal, H.M.N.; Akram, Z. Microfluidics engineering: Recent trends, valorization, and applications. *Arab. J. Sci. Eng.* **2018**, 43, 23–32. [CrossRef]
- 4. Hyun, K.A.; Lee, T.Y.; Lee, S.H.; Jung, H.I. Two-stage microfluidic chip for selective isolation of circulating tumor cells (CTCs). *Biosens. Bioelectron.* **2015**, *67*, 86–92. [CrossRef]
- 5. Gijs, M.A.; Lacharme, F.; Lehmann, U. Microfluidic applications of magnetic particles for biological analysis and catalysis. *Chem. Rev.* **2010**, *110*, 1518–1563. [CrossRef]
- 6. Yao, J.; Zhao, K.; Lou, J.; Zhang, K. Recent advances in dielectrophoretic manipulation and separation of microparticles and biological cells. *Biosensors* **2024**, *14*, 417. [CrossRef]
- 7. Buglie, W.L.; Tamrin, K.F. Enhanced mixing in dual-mode cylindrical magneto-hydrodynamic (MHD) micromixer. *Proc. Inst. Mech. Eng. Part E J. Process Mech. Eng.* **2022**, 236, 2491–2501. [CrossRef]
- 8. Hong, S.L.; Zhang, N.; Qin, L.; Tang, M.; Ai, Z.; Chen, A.; Wang, S.; Liu, K. An automated detection of influenza virus based on 3-D magnetophoretic separation and magnetic label. *Analyst* **2021**, *146*, 930–936.
- 9. Ashkezari, A.H.; Dizani, M.; Shamloo, A. Integrating hydrodynamic and acoustic cell separation in a hybrid microfluidic device: A numerical analysis. *Acta Mech.* **2022**, 233, 1881–1894. [CrossRef]
- 10. Esposito, G.; Romano, S.; Hulsen, M.A.; D'Avino, G.; Villone, M.M. Numerical simulations of cell sorting through inertial microfluidics. *Phys. Fluids* **2022**, *34*, 072009. [CrossRef]
- 11. Aldemir, A.T.; Cadirci, S.; Trabzon, L. Investigation of inertial focusing of micro-and nanoparticles in spiral microchannels using computational fluid dynamics. *Phys. Fluids* **2023**, *35*, 112012. [CrossRef]
- 12. de Timary, G.; Rousseau, C.J.; Van Melderen, L.; Scheid, B. Shear-enhanced sorting of ovoid and filamentous bacterial cells using pinch flow fractionation. *Lab Chip* **2023**, 23, 659–670. [CrossRef]
- 13. Rezaei, B.; Zand, M.M.; Javidi, R. Numerical simulation of critical particle size in asymmetrical deterministic lateral displacement. *J. Chromatogr. A* **2021**, *1649*, 462216. [CrossRef]
- 14. Nieuwstadt, H.A.; Seda, R.; Li, D.S.; Fowlkes, J.B.; Bull, J.L. Microfluidic particle sorting utilizing inertial lift force. *Biomed. Microdevices* **2011**, *13*, 97–105. [CrossRef]

Micromachines 2025, 16, 1145 11 of 11

15. Mashhadian, A.; Shamloo, A. Inertial microfluidics: A method for fast prediction of focusing pattern of particles in the cross section of the channel. *Anal. Chim. Acta* **2019**, *1083*, 137–149. [CrossRef]

- 16. Di Carlo, D.; Irimia, D.; Tompkins, R.G.; Toner, M. Continuous inertial focusing, ordering, and separation of particles in microchannels. *Proc. Natl. Acad. Sci. USA* **2007**, *104*, 18892–18897. [CrossRef]
- 17. Hur, S.C.; Tse, H.T.; Di Carlo, D. Sheathless inertial cell ordering for extreme throughput flow cytometry. *Lab Chip* **2010**, *10*, 274–280. [CrossRef]
- 18. Asghari, M.; Serhatlioglu, M.; Ortaç, B.; Solmaz, M.E.; Elbuken, C. Sheathless microflow cytometry using viscoelastic fluids. *Sci. Rep.* **2017**, *7*, 12342. [CrossRef]
- 19. Jia, Z.; Wu, J.; Wu, X.; Yuan, Q.; Chan, Y.; Liu, B.; Zhang, J.; Yan, S. Size-tunable elasto-inertial sorting of *Haematococcus pluvialis* in the ultrastretchable microchannel. *Anal. Chem.* **2023**, *95*, 13338–13345. [CrossRef]
- 20. Wang, X.; Zandi, M.; Ho, C.C.; Kaval, N.; Papautsky, I. Single stream inertial focusing in a straight microchannel. *Lab Chip* **2015**, 15, 1812–1821. [CrossRef]
- 21. Kim, U.; Kwon, J.Y.; Kim, T.; Cho, Y. Particle focusing in a straight microchannel with non-rectangular cross-section. *Micromachines* **2022**, *13*, 151. [CrossRef]
- 22. Yap, Y.; Tan, S.; Nguyen, N.; Murshed, S.; Wong, T.; Yobas, L. Thermally mediated control of liquid microdroplets at a bifurcation. *J. Phys. D Appl. Phys.* **2009**, 42, 065503. [CrossRef]
- 23. Li, H.; Wu, Y.; Wang, X.; Zhu, C.; Fu, T.; Ma, Y. Magnetofluidic control of the breakup of ferrofluid droplets in a microfluidic Y-junction. *RSC Adv.* **2016**, *6*, 778–785. [CrossRef]
- 24. Cruz, J.; Hjort, K. High-resolution particle separation by inertial focusing in high aspect ratio curved microfluidics. *Sci. Rep.* **2021**, 11, 13959. [CrossRef]
- 25. Shen, S.; Tian, C.; Li, T.; Xu, J.; Chen, S.W.; Tu, Q.; Mao, S.Y.; Liu, W.; Wang, J. Spiral microchannel with ordered micro-obstacles for continuous and highly-efficient particle separation. *Lab Chip* **2017**, *17*, 3578–3591. [CrossRef] [PubMed]
- 26. Shamloo, A.; Mashhadian, A. Inertial particle focusing in serpentine channels on a centrifugal platform. *Phys. Fluids* **2018**, *30*, 012002. [CrossRef]
- 27. Do, Q.; Van, D.; Nguyen, V.; Pham, V. A numerical modeling study on inertial focusing of microparticle in spiral microchannel. *AIP Adv.* **2020**, *10*, 075017. [CrossRef]
- 28. Palumbo, J.; Navi, M.; Tsai, S.S.; Spelt, J.K.; Papini, M. Inertial particle separation in helical channels: A calibrated numerical analysis. *AIP Adv.* **2020**, *10*, 125101. [CrossRef]
- 29. Stoecklein, D.; Di Carlo, D. Nonlinear microfluidics. Anal. Chem. 2018, 91, 296–314. [CrossRef]
- 30. Ho, B.; Leal, L. Inertial migration of rigid spheres in two-dimensional unidirectional flows. *J. Fluid Mech.* **1974**, *65*, 365–400. [CrossRef]
- 31. Wiede, A.; Stranik, O.; Tannert, A.; Neugebauer, U. Microfluidic system for cell mixing and particle focusing using dean flow fractionation. *Micro* **2023**, *3*, 671–685. [CrossRef]
- 32. Gou, Y.; Zhang, S.; Sun, C.; Wang, P.; You, Z.; Yalikun, Y.; Tanaka, Y.; Ren, D. Sheathless inertial focusing chip combining a spiral channel with periodic expansion structures for efficient and stable particle sorting. *Anal. Chem.* **2019**, 92, 1833–1841. [CrossRef] [PubMed]
- 33. Lim, J.; Yeap, S.P.; Low, S.C. Challenges associated to magnetic separation of nanomaterials at low field gradient. *Sep. Purif. Technol.* **2014**, 123, 171–174. [CrossRef]
- 34. Maxey, M.R.; Riley, J.J. Equation of motion for a small rigid sphere in a nonuniform flow. Phys. Fluids 1983, 26, 883–889. [CrossRef]
- 35. Zhu, J.; Liang, L.; Xuan, X. On-chip manipulation of nonmagnetic particles in paramagnetic solutions using embedded permanent magnets. *Microfluid. Nanofluidics* **2012**, *12*, 65–73. [CrossRef]
- 36. Lee, M.; Shin, J.; Choi, S.; Park, J. Enhanced blood plasma separation by modulation of inertial lift force. *Sens. Actuators B* **2014**, 190, 311–317. [CrossRef]
- 37. Zhang, J.; Yan, S.; Li, W.; Alici, G.; Nguyen, N. High throughput extraction of plasma using a secondary flow-aided inertial microfluidic device. *RSC Adv.* **2014**, *4*, 33149–33159. [CrossRef]
- 38. Shrestha, J.; Bazaz, S.; Ding, L.; Vasilescu, S.; Idrees, S.; Söderström, B.; Hansbro, P.; Ghadiri, M.; Warkiani, M. Rapid separation of bacteria from primary nasal samples using inertial microfluidics. *Lab Chip* **2023**, *23*, 146–156.

Disclaimer/Publisher's Note: The statements, opinions and data contained in all publications are solely those of the individual author(s) and contributor(s) and not of MDPI and/or the editor(s). MDPI and/or the editor(s) disclaim responsibility for any injury to people or property resulting from any ideas, methods, instructions or products referred to in the content.